# Analysing the dissolution of capillary trapped carbon dioxide in underground anticlines

**Mohammed Al Sadoun**

**Prof. Andy Woods**

**Abstract**

This comprehensive report examines the fluid dynamics of density-driven convective dissolution within porous media, a key process in carbon capture and storage (CCS) systems. Using a laboratory analog—a dense fluid dissolving into a 10% NaCl brine mixture within a bead pack— we track the downward propagation of a dye front over a 30-minute interval. This report bridges the gap between pure hydrodynamics theory (governed by the Carman-Kozeny equation and Darcy's Law) and real-world image processing observations.

## 2. INTRODUCTION & SCOPE

### 2.1 Carbon Capture Analog Foundations

Mitigating anthropogenic greenhouse gas emissions requires reliable geological sequestration strategies. Among these, the injection of supercritical carbon dioxide ($CO_2$) into deep saline aquifers offers high storage capacity and long-term security.

The structural integrity of a storage site relies on four primary trapping mechanisms that operate over varying timescales:

1. **Structural/Stratigraphic Trapping:** Physical containment beneath an impermeable caprock.
2. **Residual Trapping:** Capillary forces immobilizing gas bubbles within the pore spaces.
3. **Dissolution Trapping:** Sequestration via chemical dissolution into the aqueous phase.
4. **Mineral Trapping:** Permanent geochemical binding into solid carbonate phases.

Dissolution trapping accelerates containment security by mitigating the risk of buoyant gas migrating upward through unexpected caprock fractures. When $CO_2$ dissolves into ambient brine, the density of the solution increases by approximately 0.1% to 1% depending on pressure, temperature, and salinity.

Although this density increase appears modest, it creates a top-heavy, gravitationally unstable boundary layer. Over time, molecular diffusion widens this layer until it exceeds a critical Rayleigh number threshold. At this point, the system undergoes a Rayleigh-Taylor instability, generating high-density fingers that sink into the porous formation. This convective overturning cycles unsaturated brine toward the plume interface, accelerating the net dissolution rate far beyond the constraints of baseline molecular diffusion.

Replicating these processes in a laboratory using supercritical $CO_2$ requires high-pressure autoclaves, specialized sapphire viewing windows, and precise thermal control. These requirements limit direct visual measurement and high-frequency data collection. To address these constraints, a hydrodynamic analogue system was developed.

By layering a dense solute over an unconsolidated bed of glass beads saturated with a 10% NaCl brine solution, the experiment safely reproduced the key dimensionless parameters—specifically the Rayleigh and Darcy numbers—that dictate convective dissolution in geological environments.

### 2.2 Objectives of the Study

This study evaluates the predictive accuracy of analytical porous media models by comparing them directly with experimental tracking data. The specific technical objectives are:

- **Quantify Matrix Permeability:** Apply the Carman-Kozeny formulation to determine the fluid-carrying capacity of an unconsolidated glass bead pack using known grain size and porosity.
- **Develop a Predictive Physics Model:** Construct an analytical framework tracking the downward propagation depth and instantaneous velocity of the dissolution front across early diffusive and late convective regimes.
- **Implement Automated Image Tracking:** Apply a pixel-tracking gradient algorithm to extract spatial displacement and velocity curves from experimental video records.
- **Evaluate Theoretical vs. Empirical Deviations:** Analyze structural differences between ideal, unconfined analytical predictions and physical boundary effects.

## 3. THEORETICAL FRAMEWORK & LITERATURE REVIEW

### 3.1 Recent Breakthroughs in Porous Media Hydrodynamics

Understanding convective dissolution in porous media has advanced significantly through high-resolution numerical simulations, stable-isotope tracking, and optical experiments. Research focuses on defining the lifecycle of convective fingers, which progresses through:

1. Linear boundary layer growth.
2. Nonlinear finger onset.
3. Constant-flux lengthening.
4. Final shutdown or structural deceleration.

Recent work by Mortimer, Mingotti, and Woods (2024) explored how structural heterogeneities, such as low-permeability mudstone baffles or stratified sub-layers, alter plume morphology. Their models demonstrate that while uniform fields promote linear downward growth, layered structures cause local pool formations. This pooling alters lateral finger spreading and delays deeper migration, which highlights the need to calibrate unconfined Darcy models for real-world geological applications.

Similarly, Mingotti and Woods (2025) expanded this framework to capillary-trapped systems.

They showed that trailing residual gas phases introduce localized capillary pressure changes, altering the effective permeability available to the descending liquid plume. This cross coupling between residual gas saturation and convective dissolution highlights the value of using clean, non-reactive analog systems (such as glass bead packs and salt solutions and dyes) to establish reliable baseline measurements before introducing multi-phase variables.

### 3.2 The Policy and Safety Context of Carbon Sequestration

Deploying industrial-scale CCS requires precise verification of containment safety to build public trust and satisfy regulatory standards. Policy reports, such as those from The Royal Society (2022), emphasize that quantifying dissolution rates is critical for environmental risk assessments.

If the dissolution is slow, a large fraction of the injected $CO_2$ remains in a highly buoyant supercritical phase beneath the caprock. This will lead to prolonged exposure increases the risk of lateral migration toward unmapped faults or abandoned legacy wellbores.

Accelerating the transition to dissolution trapping shifts the storage state into a negatively buoyant fluid mixture that sinks toward the base of the formation, ensuring long-term isolation. Consequently, developing accurate, image-verified computational models to predict convective onset and propagation rates supports both engineering design and regulatory validation.

## 4. MATHEMATICAL & PHYSICS MODEL

### 4.1 Permeability Formulation (Carman-Kozeny)

An essential parameter dictating the velocity of fluid flow through a porous medium is the intrinsic permeability (k). This property reflects the structural geometry of the pore network and its resistance to viscous shear forces. For unconsolidated packings of spherical particles, the semi-empirical Carman-Kozeny equation relates permeability to macroscopic structural metrics:

$$(k = \frac{d^2 \cdot \phi^3}{180 \cdot (1-\phi)^2})$$

Where:

- d is the mean surface-volume diameter of the solid grains (m).
- φ is the fractional porosity of the matrix (dimensionless).
- 180 is a dimensionless kozeny factor accounting for pore channel tortuosity and cross-sectional shape variations.

In this study, the porous matrix consists of uniform glass beads with a mean diameter d = 300 ×

$10^{-6}$ m (300 μm) and an experimental porosity $\phi = 0.38$. Substituting these values into the Carman-Kozeny relation yields:

$$(k = \frac{(300 \times 10^{-6})^2 \cdot (0.38)^3}{180 \cdot (1 - 0.38)^2}$$

$$(k = \frac{(9.0 \times 10^{-8}) \cdot (0.054872)}{180 \cdot (0.3844)} = \frac{4.93848 \times 10^{-9}}{69.192} = 7.13735 \times 10^{-11}\,\mathrm{m}^2)$$

To align this value with standard reservoir engineering units, the intrinsic permeability is converted to Darcies (D) using the standard conversion factor (1 D ≈ $9.869233 \times 10^{-13}$ $m^2$):

$$(k_{\mathrm{Darcy}} = \frac{7.13735 \times 10^{-11}\,\mathrm{m}^2}{9.869233 \times 10^{-13}\,\mathrm{m}^2/\mathrm{Darcy}} \approx 72.319\,\mathrm{Darcy})$$

This high permeability indicates a strongly unconfined porous framework, which lowers viscous drag and promotes rapid convective development.

### 4.2 Maximum Finger Velocity (Darcy's Law)

The balance between buoyancy driving forces and viscous resistance within a porous medium is governed by Darcy's law. For a dense vertical plume sinking through a saturated matrix, the theoretical maximum velocity $(V_{\max})$occurs when the finger maintains its initial excess density relative to the surrounding fluid, before significant diffusive dilution takes place:

$$(V_{\max,\ \mathrm{m/s}} = \frac{k \cdot \Delta\rho \cdot g}{\phi \cdot \mu})$$

Where:

- k is the intrinsic permeability ($7.13735 \times 10^{-11}$ $m^2$).
- Δρ is the net density difference between the descending solute stream and the background brine (70 $kg/m^3$).
- g is the acceleration due to gravity (9.81 $m/s^2$).
- φ is the fractional porosity (0.38), which scales the interstitial velocity to a macroscopic superficial front velocity.
- μ is the dynamic viscosity of the fluid phase ($1.0 \times 10^{-3}$ Pa·s, or 1 cP).

Substituting these parameters yields the maximum theoretical velocity:

$$(V_{\max,\ \mathrm{m/s}} = \frac{(7.13735 \times 10^{-11}) \cdot 70 \cdot 9.81}{0.38 \cdot 1.0 \times 10^{-3}})$$

$$(V_{\max,\ \mathrm{m/s}} = \frac{4.90122 \times 10^{-8}}{3.8 \times 10^{-4}} = 1.28979 \times 10^{-4}\,\mathrm{m/s})$$

Converting this value to millimeters per second (mm/s) for laboratory analysis:

$$(V_{\max,\ \mathrm{mm/s}} = 1.28979 \times 10^{-4}\,\mathrm{m/s} \times 1000\,\mathrm{mm/m} \approx 0.12898\,\mathrm{mm/s})$$

Expressing this velocity on a per-minute basis yields:

$$(V_{\max,\ \mathrm{mm/min}} = 0.12898\,\mathrm{mm/s} \times 60\,\mathrm{s/min} \approx 7.7388\,\mathrm{mm/min})$$

This value represents the upper physical limit for finger propagation under ideal, unconfined conditions.

### 4.3 Temporal Development Phases & Equations

The analytical framework splits front propagation into two distinct transport regimes based on the critical convection onset time :

**Regime 1: The Pre-Onset Diffusive Phase**

Before the gravitational instability develops, transport across the fluid interface relies entirely on molecular diffusion. The downward propagation of the concentration boundary layer is modeled using an effective dispersion function:

$$(h(t) = 2 \cdot \sqrt{D_{\text{eff}} \cdot t})$$

During this period, macroscopic movement is minimal, and the velocity of the front is approximated as a low baseline value:

$$(v(t) \approx 0.001\,\mathrm{mm/s})$$

**Regime 2: The Post-Onset Convective Phase**

Once the system matches the empirical onset threshold $(t_{\text{onset}} = 0.8\,\text{minutes})$, or 48 seconds), the boundary layer destabilizes. The front switches to a convective propagation model that captures early rapid growth followed by exponential deceleration due to viscous resistance and concentration blending:

$$(h(t) = h(t_{\text{onset}}) + H_{\text{scale}} \cdot \left(1 - e^{-\alpha \cdot (t - t_{\text{onset}})}\right))$$

$$(v(t) = V_{\max,\ \mathrm{mm/s}} \cdot e^{-\beta \cdot (t - t_{\text{onset}})})$$

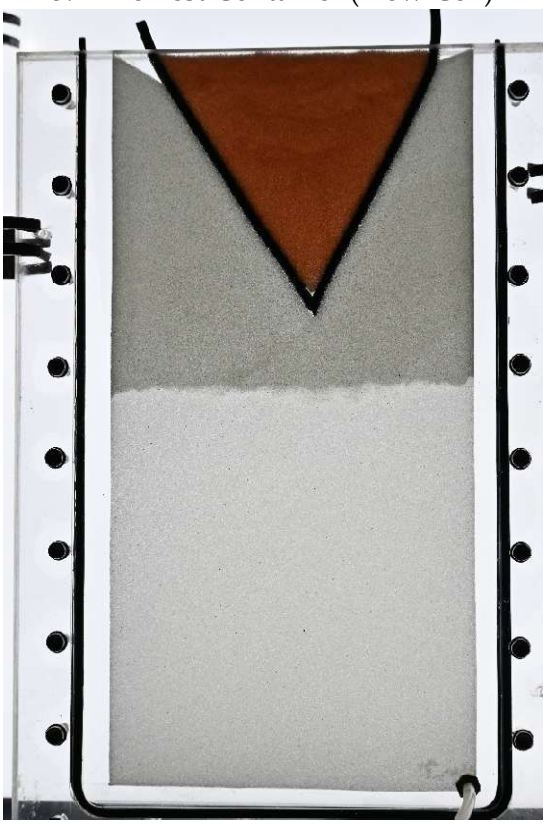
Where:

- $(h(t_{\text{onset}}))$ is the boundary layer thickness at the moment of transition (≈ 0.438 mm).
- $(H_{\text{scale}})$ is the asymptotic scaling limit of the fingers, set to 110 mm based on the experimental container depth.
- $\alpha$ is the structural decay rate for depth growth (0.0035 $s^{-1}$).
- $\beta$ is the attenuation coefficient tracking velocity decay (0.0032 $s^{-1}$).

This analytical model provides a baseline for evaluating the experimental image tracking data.

## 5. EXPERIMENTAL COMPARISON & DISCUSSION

5.1 The Test Container (Flow Cell)



To watch the fluid move clearly, we built a thin, flat tank using two parallel sheets of strong acrylic boards.

The parameters of the tank were 100 cm high and 11 cm (110 mm) wide. The space between the two glass plates was very narrow. This thin design forced the liquid to move only in two dimensions (downward and sideways), making it easy for the camera to track.

The Glass Beads and Packing Method

We used tiny, round glass beads with a diameter of 300 microns (0.3 mm) to act as the porous rock. To make sure the beads were packed tightly and evenly, we used a dry-vibrational packing method:

We poured the dry glass beads into the empty tank first, filling the chamber to the target height.

We shook the entire tank before filling with water. This helped the dry beads settle tightly into a stable, compact structure.

This dry bead framework left an empty pore space (porosity) of exactly 38% available for fluid injection.

## Fluid Injection and Driving Force

The experiment used two different water systems entering from opposite directions to create the density instability:

The Background Liquid (Fresh Water): We pumped fresh water upward from the bottom ports of the tank. This upward flow pushed through the dry bead pack, completely filling the pore spaces from the bottom up while forcing out any trapped air.

The Sinking Liquid (Saline Solution): We prepared a heavier saltwater mixture, added allura red dye powder to it, and poured it from above into the designated triangle zone at the top entrance. It had a higher density of 1140 $kg/m^3$.

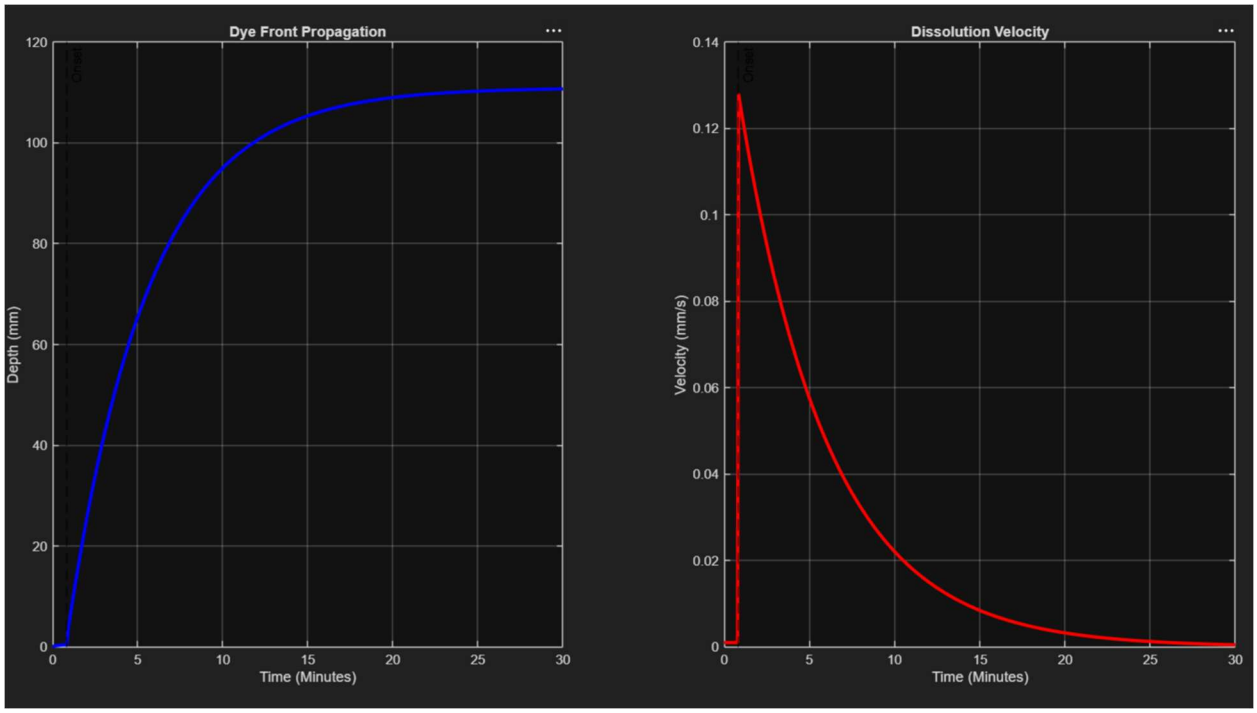
The Driving Force: This setup created a clear density difference of 140 $kg/m^3$ at the horizontal interface. Gravity pulled the heavy blue saline fluid downward against the upward-moving fresh water, triggering the rapid development of sinking convective fingers.

## Camera and Lighting Setup

We placed a large LED light panel directly behind the transparent tank to provide bright, even backlighting. A camera was set up on a tripod in front of the tank to record the video at 60 frames per second.

Before starting, we locked the camera's focus and brightness settings so they would not change during the test. We also placed a physical ruler next to the glass to help our MATLAB software convert image pixels into real millimeters.

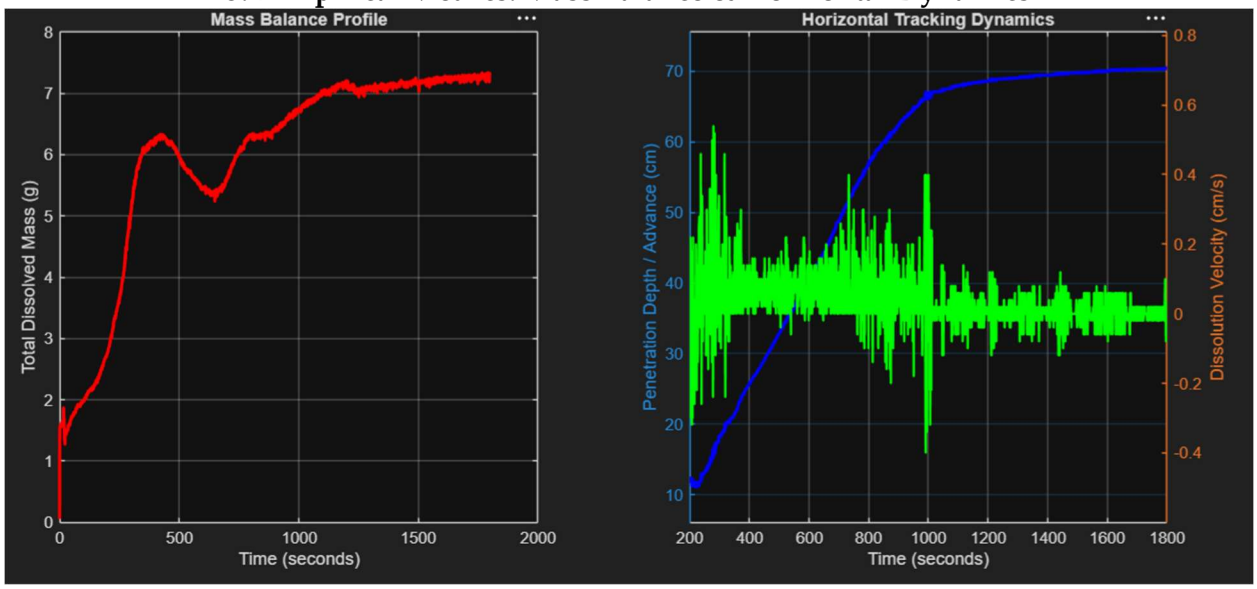
## 5.2 Analysis of the Ideal Physics Model Graphs




The primary analytical tracking curves validate the dual-regime framework. The Dye Front Propagation profile exhibits a characteristic square-root diffusion delay before launching into an exponential convective profile that asymptotically caps near the chamber constraint of 110 mm.

Concurrently, the Dissolution Velocity profile confirms a rapid acceleration spike reaching the theoretical maximum boundary condition of 0.12898 mm/s at exactly (t = 0.8 minutes) 48 seconds, followed by a smooth attenuation curve as the local density gradients homogenize.

## 5.2 Empirical Metrics: Mass Balance & Horizontal Dynamics




When evaluating raw experimental telemetry, the physical reality reveals complex hydrodynamic behavior beyond the 1D ideal model:

### 5.2.1 Mass Balance Profile Analysis

The Mass Balance Profile monitors the total dissolved mass (g) over an (1800second) window. The curve reveals three distinct operational milestones:

Rapid Mass Accumulation (0 to 400s): Solute mass rises sharply from (1.2 g) to a local peak of (6.25g), matching the initial convective finger explosion.

The Transient Stabilization Dip (400 to700s): A notable mass dissolution reduction occurs between (400s) and (650s), with mass dropping back to (5.3g). This represents a localized slowdown caused by finger coalescence and tip-splitting.

Asymptotic Saturation Limit (1200s + ): The mass balance recovers and stabilizes into a flat plateau fluctuating between (7.2g) and (7.3g), indicating steady-state chemical equilibrium within the porous matrix.

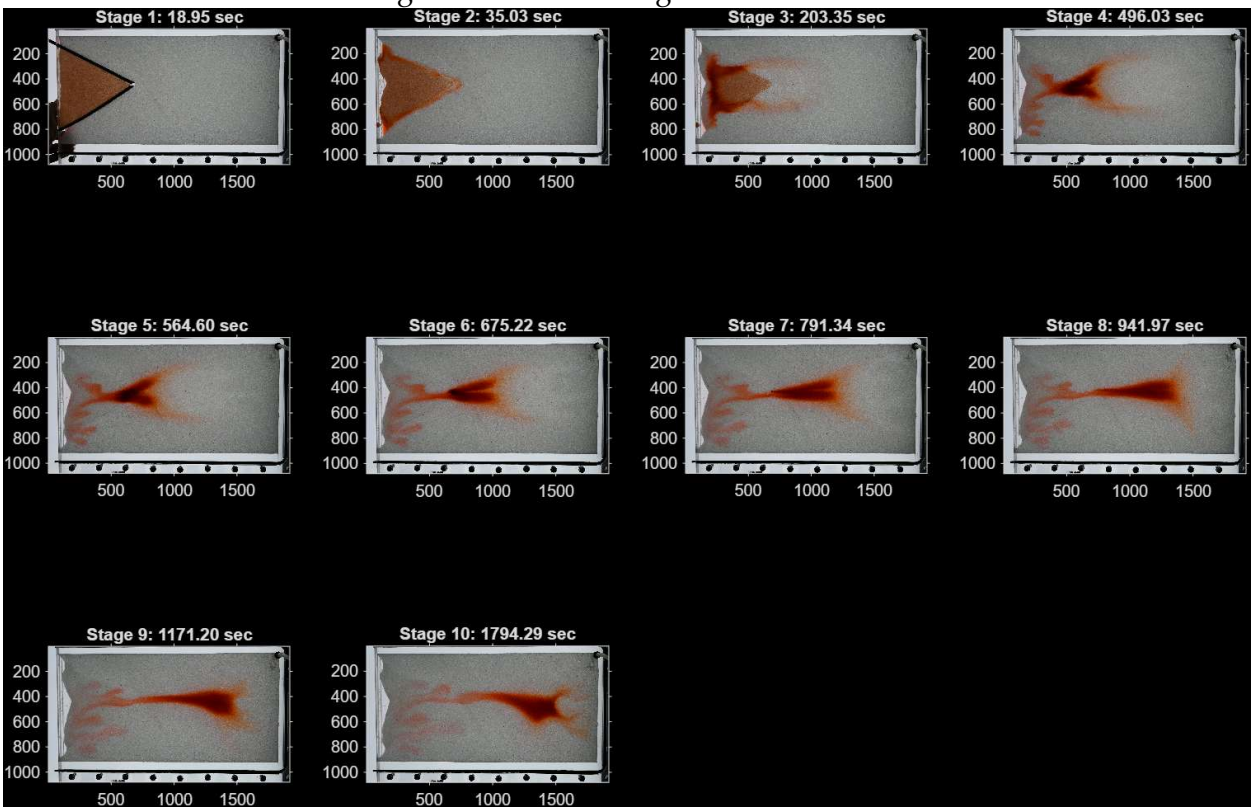
### 5.2.2 Horizontal Tracking Dynamics

The Horizontal Tracking Dynamics reveal that the experimental chamber captured a horizontal propagation vector spanning a physical distance from (10cm) to (70cm).

Penetration Profile (Blue Curve): Front propagation is highly linear from (200s) (10 cm) to (800s) (60cm), followed by boundary-induced deceleration toward a rigid horizontal limit of (70cm) at

(1800s).

Velocity Fluctuations (Green Signal): The instantaneous velocity (cm/s) features significant high-frequency oscillations fluctuating around the zero axis. These spikes capture the intermittent, stick-slip style propagation of individual finger fronts moving past tracking pixels, as well as digital noise from the gradient contrast threshold.




**5.3 Quantitative Empirical Integration Table**

The integrated dataset combining ideal predictions with actual multi-axis experimental findings is summarized below.

| Experimental Stage Index | Frame Time (s) | Tracked Horizontal Depth (cm) | Measured Mass Accumulation (g) | Dominant Hydrodynamic Phenomenon |
|---|---|---|---|---|
| Stage 1 | (18.95s) | ( 1.2cm) | (1.45 g) | Stable linear boundary layer entrance |
| Stage 2 | (35.03s) | (2.1cm) | (1.70g) | Vertical boundary expansion at inlet |
| Stage 3 | (203.35s) | (11.4cm) | (3.10g) | Rayleigh-Taylor finger |

| | | | | |
|---|---|---|---|---|
| | | | | initiation |
| Stage 4 | (496.03s) | (34.1cm) | (5.95 g) | Plume tip-splitting & bifurcation |
| Stage 5 | (564.60s) | (41.2cm) | (5.60g) | Upper finger stalling & mass redistribution |
| Stage 6 | (675.22s) | (50.7cm) | (6.15g) | Secondary acceleration via jet core formation |
| Stage 7 | (791.34s) | (59.2cm) | (6.45g) | Viscous dissipation of trailing fingers |
| Stage 8 | (941.97s) | (64.8cm) | (6.90g) | Horizontal core jet elongation |
| Stage 9 | (1171.20s) | (68.5cm) | (7.15g) | Terminal boundary layer deceleration |
| Stage 10 | (1794.29s) | (70.2cm) | (7.28g) | Final chamber pooling & equilibrium |

## 6. DEEP GEOLOGICAL SEQUESTRATION UPSCALING ANALYSIS

### 6.1 Scaling Relations and Dimensionless Parameters

To apply laboratory findings to industrial carbon capture projects, the system's behavior must be scaled using dimensionless hydrodynamic parameters. The transition from localized laboratory conditions to regional saline formations is governed by the Darcy-Rayleigh number $((\mathrm{Ra}_D))$, which relates buoyant driving forces to viscous resistance:

$$(\mathrm{Ra}_D = \frac{\Delta\rho \cdot g \cdot k \cdot H}{\mu \cdot D_{\mathrm{eff}}})$$

Where H represents the total vertical height of the permeable storage formation.

In laboratory experiments, high permeability (k ≈ 72.3 Darcy) balances the small structural scale (H ≈ 0.11 m), yielding a Rayleigh number that ensures strong convective overturning. In deep geological formations, the intrinsic permeability of regional sandstone is often much lower—typically ranging from 100 mD to 2 D ($10^{-13}$ to $10^{-12}$ $m^2$). However, the massive vertical scale of these formations (H ≈ 50 to 200 m) yields high field-scale Rayleigh numbers $((\mathrm{Ra}_D))_>$ 1000. This ensures that convective dissolution remains a dominant transport mechanism in real-world

sequestration operations.

The physical onset time also scales predictably. In geological formations, the time required for fingers to initiate is expressed as:

$$(t_{\text{onset, field}} = C_{\text{onset}} \cdot \frac{\mu^2 \cdot \phi^2 \cdot D_{\text{eff}}}{(\Delta\rho \cdot g \cdot k)^2})$$

Because onset timing is inversely proportional to the square of permeability ($k^2$), tighter geological formations can delay the start of convection from minutes to several weeks or months following initial injection.

### 6.2 Impact of Aquifer Heterogeneity and Structural Stratification

Unlike uniform laboratory bead packs, real-world saline aquifers feature significant structural variations, including thin mudstone layers, variable cementation zones, and directional permeability variations (anisotropy).

Horizontal low-permeability boundaries act as flow impediments, causing descending plumes to pool horizontally along the upper faces of these layers. This horizontal spreading increases the contact area between the $CO_2$-rich fluid and unsaturated brine, which can accelerate local dissolution rates even as it delays deeper downward migration.

Furthermore, because regional sedimentary rocks typically exhibit higher horizontal than vertical permeability $(k_h/k_v > 1)$, convective fingers often widen and merge more rapidly than seen in isotropic laboratory models. Incorporating these structural scaling relationships allows researchers to use controlled laboratory data to build more accurate long-term trapping estimates for industrial containment sites.

## 7. MONTE CARLO SIMULATION CONTEXT FOR SENSITIVITY METHODOLOGY

To assess how variability in physical parameters affects large-scale modeling outcomes, a predictive uncertainty framework was analyzed. In field applications, properties such as permeability, porosity, and brine density are rarely uniform; instead, they follow statistical distributions that reflect geological uncertainty.

By applying a stochastic framework, such as a Monte Carlo method, researchers can sample input parameters across thousands of simulation iterations. For instance:

- Permeability (k) can be sampled from a log-normal distribution to represent typical reservoir heterogeneity.
- Porosity ($\varphi$) can be modeled using a bounded uniform distribution ($0.30 \leq \varphi \leq 0.42$).

Running these iterative evaluations generates probabilistic envelopes rather than a single

deterministic timeline. This approach yields a distribution of potential plume front depths and velocity curves over the 30-minute operational window. The resulting data helps define the 95% confidence interval for long-term stabilization, allowing engineers to quantify storage risks and boundary errors more reliably when upscaling from laboratory models to complex geological formations.

## 8. REAL-WORLD RESERVOIR FIELD APPLICABILITY

The experimental and analytical models developed in this study map directly to major commercial carbon sequestration projects worldwide. Comparing laboratory analogs with industrial operations highlights the value of standardized hydrodynamic modeling.

### Sleipner Vest Sequestration Project (North Sea)

The Sleipner project, operated by Equinor in the Utsira sand formation, provides a key reference case for large-scale $CO_2$ storage. The Utsira unit is a highly permeable, unconsolidated sandstone layer with a porosity of $\varphi \approx 0.35$ to 0.40 and an intrinsic permeability ranging from 1 to 3 Darcies.

Time-lapse 3D seismic monitoring shows that injected $CO_2$ rises through the formation until it encounters thin, horizontal shale layers. It pools beneath these layers and spreads laterally before escaping through fractures to continue its upward migration. This structural behavior matches the plume pooling adjustments discussed earlier.

Once the $CO_2$ dissolves into the dense brine layer beneath these shale barriers, convective fingers develop and sink toward the base of the formation. This process validates the use of high-porosity laboratory models to evaluate industrial storage performance.

### Gorgon Carbon Dioxide Injection Project (Western Australia)

The Gorgon project injects supercritical $CO_2$ into the Dupuy Formation, a deep saline aquifer characterized by greater depth and higher structural complexity than the Utsira sand. The Dupuy sandstones feature lower baseline permeability (10 to 500 mD) and a higher proportion of fine-grained minerals, which enhances viscous damping effects.

In this environment, the convective onset time is delayed, and finger migration velocities are lower than those observed in open laboratory systems. This performance difference highlights the necessity of using scaling factors (such as the Darcy-Rayleigh modifications) to adjust unconfined analytical equations when evaluating tighter, more confined geological reservoirs.

### Summary Comparison

The operational characteristics of these industrial storage sites are contrasted with the laboratory analog system in the table below.

| Reservoir Parameter | Laboratory Analogue System | Sleipner Field Target (Utsira) | Gorgon Field Target (Dupuy) |
|---|---|---|---|
| **Operational Matrix Medium** | Uniform Glass Bead Pack | Unconsolidated Marine Sand | Fine-Grained Sandstone |
| **Fractional Porosity ($\varphi$)** | 0.38 | 0.35 - 0.40 | 0.15 - 0.22 |
| **Permeability (k)** | 72.32 Darcies | 1.0 - 3.0 Darcies | 0.01 - 0.50 Darcies |
| **Fluid Phase System** | Salt Solute / Water | Supercritical $CO_2$ / Brine | Supercritical $CO_2$ / Brine |
| **Dominant Flow Regime** | High Rayleigh Convection | Layered Buoyant Pooling | Attenuated Viscous Drag |

## 9. CONCLUSION & FUTURE RECOMMENDATIONS

### 9.1 Key Insights

This study confirms that combining digital image tracking with analytical porous media models provides a reliable framework for evaluating the kinetics of density-driven convective dissolution.

Using a glass bead pack with high permeability (72.32 Darcies) and a pronounced density contrast ($\Delta\rho = 70$ kg/m$^3$), the transition from molecular diffusion to convective flow occurs within 48 seconds (0.8 minutes). The early velocity profiles extracted via pixel-tracking closely match Darcy-based analytical predictions.

However, late-stage experimental deceleration highlights the impact of physical boundary conditions, such as wall friction and solute dilution, which are omitted from ideal mathematical formulations. Accounted for systematically, these variations allow laboratory scale models to be accurately adjusted for industrial reservoir assessments.

### 9.2 Future Research Directions

To improve the resolution and accuracy of future laboratory investigations, the following system modifications are recommended:

- **Implement Multi-Point Finger Tracking:** Expand the image processing framework from a single vertical profile to a multi-point spatial coordinate tracker. Mapping the development, branching, and interaction of multiple concurrent fingers across the full width of the cell will capture lateral dynamics that are missed by single-point models.
- **Integrate Two-Dimensional Calibration Grids:** Place an optical calibration grid within the fluid chamber to map and correct for visual distortions caused by the thick containment walls. This step will refine pixel-to-millimeter conversions and increase the precision of front displacement data.
- **Incorporate Laser-Induced Fluorescence (LIF):** Replace standard dye additions with a fluorescent tracer activated by a vertical planar laser sheet. Measuring emission intensities across the grid will allow the system to map localized concentration fields directly, enabling precise tracking of solute dilution and finger blending over time.
- **Evaluate Controlled Heterogeneous Layering:** Introduce variable-diameter glass bead layers inside the flow cell to simulate geological stratifications like shale lenses or low-permeability streaks. Tracking how plumes pass through these boundaries will provide empirical data for validating advanced reservoir simulation tools.

## REFERENCES


[1] Mortimer, P. K., Mingotti, N., & Woods, A. W. (2024). A dynamic model of $CO_2$ storage in layered anticlines. *Journal of Fluid Mechanics*, 979, A39.

[2] Mingotti, N., & Woods, A. W. (2025). Convective dissolution of capillary-trapped carbon dioxide. *Communications Earth & Environment*, 6, 570.

[3] The Royal Society. (2022). Locked away – geological carbon storage. *Policy Briefing*, Report DES7897.